Iterative method for optical modelling of perovskite-based tandem solar cells

E Raoult, R Bodeux, S Jutteau, S Rives, A Yaiche, A Blaizot, D Coutancier, J Rousset, S Collin

Iterative method for optical modelling of perovskite-based tandem solar cells

E. Raoult, [1,2,3,*] R. Bodeux,[1,2] S. Jutteau,[1,2] S. Rives,[1,2] A. Yaiche,[1,2] A. Blaizot,[2] D. Coutancier,[2,4] J. Rousset,[1,2] and S. Collin [2,3]

[1]*EDF R&D, 18, Boulevard Thomas Gobert, 91120, Palaiseau, France*
[2]*Institut Photovoltaïque d'Ile de France (IPVF), UMR 9006,18 Boulevard Thomas Gobert, 91120 Palaiseau, France*
[3]*Centre for Nanoscience and Nanotechnology (C2N), CNRS, Université Paris-Saclay, 91120 Palaiseau France*
[4]*CNRS, UMR 9006, 18, Boulevard Thomas Gobert, 91120 Palaiseau, France*
**emilie.raoult@edf.fr*

Abstract (max 100 mots): We present an iterative method to model the optical properties of a complete semitransparent perovskite solar cell. It is based on spectroscopic characterizations and accounts for porosity and incoherence effects. We provide the complex refractive indices of each layer, and we identify the main sources of optical losses. The optical model is also coupled to an electrical model of 4T perovskite/silicon tandem solar cells. It allows to evaluate the interplay between the optical and electrical losses, and the balance between the efficiency of the top and bottom cells. These models provide an effective way to design future tandem devices.

1. Introduction

The cumulative installed solar photovoltaics power capacity reached more than 630 GW in 2020, representing an increase by a factor of 15 during the last 10 years. However, the silicon-based solar cells that dominate the current market are getting closer and closer to the single-junction Shockley-Queisser limit, around 29.4% [1]. The most promising and successful approach to overcome this limit is the tandem architecture associating a silicon bottom cell and perovskite top cell [2].

Perovskite is a highly regarded class of material to be included as a light absorber in a semitransparent top solar cell structure. Synthesized for the first time in 2009 by Kojima et al [3], its development has been extremely rapid and it has now reached an efficiency of 25.5% for a single junction solar cell [4]. Interestingly, perovskite semiconductors have an adjustable bandgap between 1.2 and 2.2 eV when modifying its composition and are regarded as a promising option for low-cost 2- or 4-terminals (2T/4T) tandems. Recently, a 2T perovskite/silicon tandem solar cell reached an efficiency of 29.5% [4]. In comparison, the record efficiency for a 4T tandem perovskite/silicon is 29.2%, reached by the consortium European Solliance Solar Research, with a semi-transparent perovskite cell and a filtered IBC-SHJ silicon efficiencies measured at 17.8% and 11.4% respectively [4].

To build an efficient tandem, the perovskite top cell must maintain optimal electrical properties while keeping maximum transparency below its band gap. 2T tandem structures maintain good IR transmission towards the silicon cell by reducing the number of interfaces and layers such as transparent conductive oxide (TCO) known for their parasitic absorption. On the other hand, 4T tandem structures allow to use the best manufacturing processes and the most adapted layers for each cell while respecting their constraints related to the temperature, the roughness of the substrate, the solvent used and the chosen polarity (type n-i-p or p-i-n). Moreover, under operation each cell can work at its maximum power point because the

electrical systems are completely separated. 4T tandem devices are therefore more resilient to light variations [5–7].

With this in mind, a 4T tandem composed of a triple cation perovskite cell and a commercially available Aluminium Back Surface Field (Al-BSF) silicon cell was synthesized in our laboratory and reached an efficiency of 21.7% with a perovskite cell at 16.6% and a filtered silicon cell at 5.1% [8]. The spectral response of the silicon cell as well as the infrared transmission of the semitransparent perovskite cell shows significant optical losses that limit the efficiency of the device. In order to identify their origin, numerical simulations based on the propagation of optical waves in planar layers have been performed by several groups [9–17]. They are used to tune the thickness of each layer [15,17], to test different materials [10], or to adapt the perovskite bandgap to 2T or 4T tandem solar cells [10–13].

However, their use is often hindered by the lack of accurate data for the complex refractive indices of each layer constitutive of the device, i.e. the triple cation perovskite, the spiro-Ometad extraction layer or the unannealed and amorphous Indium Tin Oxide (ITO) deposited on the top of the perovskite absorber. Indeed, the optical indices of a thin layer such as ITO can depend on the deposition and post-treatment conditions such as annealing. Moreover, different compositions of the perovskite layer as $CH_3NH_3PbI_3$ (MAPbI) [12], $NH_2CH{=}NH_2PbI_3$ (FAPbI) [18], $CH_3NH_3PbI_{3-x}Cl_x$ (MAPbCl) [13] or $Cs_y(NH_2CH{=}NH_2)_{1-y}Pb(Br_xI_{1-x})_3$ (CsFAPbBrI) [11] can be used, impacting the optical properties of the whole cell. In addition, Jiang et al. have highlighted discrepancies in the optical indices values considered by different groups using a similar MAPbI perovskite deposited by spin-coating [10]. A reliable determination of the refractive index of perovskite layers is still highly needed to be implemented in the optical simulation of complete solar cells. This becomes particularly relevant for the complex high band gap perovskite composi0tion, as triple cations perovskite $Cs_{0.05}((CH_3NH_3)_{0.166}(NH_2CH{=}NH_2)_{0.833})_{0.95}Pb(Br_{0.166}I_{0.833})_3$ (CsMAFAPbIBr), that are used in semitransparent top cell of a tandem device.

In this paper, we present a comprehensive iterative method to model the optical properties of a complete semitransparent perovskite solar cell. It is based on the experimental characterization of the optical properties of the PV devices (EQE, reflection and transmission, absorption, and reflection spectra) and of each layer separately using various spectroscopic techniques. Porosity and incoherence effects are considered, and the dispersion models are refined in an iterative way until the numerical results are in good agreement with the complete dataset. As a result, we provide accurate values for the complex refractive indices of each layer, and we identify and quantify the main sources of optical losses in the top perovskite solar cell. The accuracy of these results will be put into perspective with simulations based on literature data and without the use of the iterative method presented in this work. Further improvements would require more transparent electrode layers, resulting in a trade-off between transparency and conductivity, and a balance between the performances of the top and bottom cells, respectively. Indeed, the transparency and conductive properties of Transparent Conductive Oxides (TCO) are in opposition, the improvement of one of these two parameters will most often be in spite of the other. The optical model is coupled to a simple electrical model to predict these effects and the performances of 4T perovskite/silicon tandem solar cells.

2. Experimental details

2.1 Synthesis of experimental the PV devices

The semitransparent perovskite top cell stack used for the 4T tandem is represented in Fig.1.A and B. The detailed synthesis of each layer is described in references [19,20]. A compact-mesoporous TiO_2 bilayer is firstly deposited at 450 °C on a commercial FTO covered glass substrate (TEC7 -Solems) composed of fluorine-doped SnO_2 (FTO) coated on a soda-lime glass (thickness: 3 mm). The triple cation perovskite solution $Cs_{0.05}(MA_{0.166}FA_{0.833})_{0.95}Pb(Br_{0.166}I_{0.833})_3$ is deposited on TiO_2 by spin coating and annealed at 100°C. Films of Spiro-OMeTAD and ITO are subsequently deposited on the top of the

perovskite layers by spin coating, and by RF magnetron sputtering respectively. Finally, a gold contact is thermally evaporated on ITO as shown on the cell photograph in Fig.1.C.

For specific characterizations of the opto-electrical properties of individual layers, TiO_2, perovskite, spiro-OMeTAD or ITO are synthesized on soda-lime glass using the same processes as for a complete solar cell. For the substrate TEC7, the top layer of FTO is removed by the combination of hydrochloric acid (HCl) solution and zinc powder to obtain the sample called "etched TEC7", composed by three layers: Glass, SnO_2 and SiO_2.

The silicon cell is an Al-BSF device. The original cell of 156 × 156 mm^2 was downsized by creating smaller samples with 1 cm^2 active area (including 6 metallic fingers). Then, two electrical wires were soldered on the front and back of the reduced Si cell to keep access to bottom cell contacts when top cell was stack over.

2.2 Characterization

Perovskite solar cells are measured in superstrate configuration, the cell is illuminated by the glass. I-V characteristics are measured using a digital source meter (Keithley 2400) for bias voltages between -0.2 V and 1.2 V with a sweeping rate of 20 $mV.s^{-1}$. A AM1.5G solar illumination is obtained with an AAA sun simulator (Oriel Sol3A). Semitransparent cells have an active area of 0.16 cm^2 (corresponding to the pink square visible on the cell image in Fig.1.C) and a black metallic mask is used to illuminate only 0.09 cm^2 in order to avoid the gold finger shading on the silicon cell. The External Quantum Efficiency (EQE) is measured between 300 and 850 nm for perovskite cells, and between 300 and 1200 nm for the silicon cell using an Oriel IQE200 system connected with a source meter (Keithley 2400). An Uvisel 2 ellipsometer from Horiba is used to measure the optical parameters of the different layers of the perovskite cell. The measurement is made for photon energies between 0.68 and 5.4 eV with an integration time of 300 ms and a step of 0.02 eV. The spot size is 2030*705 μm^2 with an angle of 70°. The software DeltaPsi2 developed by Horiba is used to analyze the data. To access the thicknesses of the different layers, cross-section images are carried out with a Scanning Electron Microscope (SEM - ZEISS Leo Supra 35 field emission gun (FEG) with 15 kV voltage). Thicknesses are also measured with a profilometer (Dektak). Roughness is determined by Atomic Force Microscopy (Agilent – Picosun 300) mapping, with a probe ACT from Appnano. A spectrophotometer (Agilent - Cary 5000) is used to measure the transmission (T) and the reflection (R) spectra between 200 and 1300 nm. The absorption (A) is obtained from:

$$A(\lambda) = 100\% - R(\lambda) - T(\lambda) \quad (1)$$

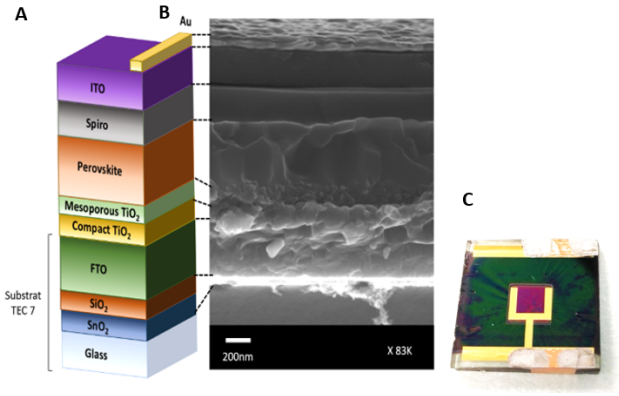

Fig. 1.A. Sketch and B. SEM cross-section image of a semitransparent perovskite cell. C. Photograph of a semitransparent perovskite cell in substrate configuration. The pink square corresponds to the cell covered by an ITO layer and defines the active area (5x5 mm^2 including the U-shaped gold contact).

3. Determination of the optical indices of the different layers

3.1 Method

An iterating process described in Fig.2 was used to build an optical model that matches well to our actual perovskite cells. The first step "A" focused on the determination of the optical index (real part n(λ) and extinction coefficient k(λ)) of each layer of the structure. Each layer was deposited on glass and its thickness and roughness are measured with a profilometer and a SEM cross-section image.

Then ellipsometry measurements are performed and analyzed to create a model of the complex optical indices. Different dispersion models listed in Table I are chosen according to the material nature (dielectric, wide-bandgap material, TCO, semiconductor absorber). The value of the least square error coefficient X^2 obtained after an iterative procedure indicates the good agreement between the model and the experimental data. In principle, there is no target value for X^2, which would depend on materials, stack complexity and morphology. The value of X^2 must be evaluated on a case by case basis. However, we consider here that X^2 lower than 15 for complex stacks or materials is acceptable, and lower than 5 for simple layers. It should be noted that the ellipsometry analysis only guarantees that the values obtained for indices, thickness and roughness allow to reach a local minimum for X^2. The thickness can be measured experimentally with a profilometer and can be bounded quite finely in the ellipsometric model. Ellipsometric simulation of roughness is based on effective medium and not on experimental values i.e. Root Mean Square (RMS) or Sa which can be obtained by AFM or confocal microscope respectively. Thus, roughness has to be adjusted using the iterative process as the optical indices.

The optical indices extracted from the fit are subsequently used in a MATLAB code developed by the McGehee group at Stanford University [21] and based on the Transfer Matrix Method (TMM) to model the transmission, reflection and absorption of the structure. The simulated spectra are compared with the experimental ones measured by spectrometry experiments. The result is considered as acceptable if the Mean Absolute Error (MAE) is smaller than 3%, see the results in Table II. If the MAE is above 3%, the values of indices, thickness and roughness in the optical model used to fit ellipsometry measurements are modified until reaching a new minimum for X^2, and the TMM simulations are repeated until a good match is obtained. There is no number of iterations to perform to reach a MAE above 3%, it is just a matter of finding the right set of values (indices/thickness/roughness). As an example, Fig. S1 shows a diagram of the evolution of X^2 and MAE as a function of the number of iterations with the perovskite layer on glass. The optical indices for the perovskite layer are those obtained in iteration #10 because they allow a MAE value below 3%, although it is not the iteration with the lowest X^2 or the last one performed.

This iterating process and the implementation of the roughness of interfaces and incoherence of thick layers allow us to refine our results compared those previously published [19,20]. A better agreement between the model and the experimental data was also obtained by the used of new dispersion models.

Once the results are satisfactory for every layer, the optical indices can be used to model the complete perovskite solar cell, see Fig.2.B with a similar method as described above. However, in that case, the optical indices of the different layers are considered similar to those deposited on glass. Thus, the iteration is done only on the TMM simulation by modifying slightly the thicknesses of the layer according to the SEM cross-section measurements, and the roughness of interfaces. As before, the results are in good agreement with the experimental measurement and are discussed in Section 4. As before, the results are in good agreement with the experimental measurement and are discussed in Section 4. Ellipsometry models and fits, as well as simulated and experimental transmission, reflection and absorption spectra for each layer are provided in the supplementary data (Fig. S1 and S2) and compared to models without the iterative method.

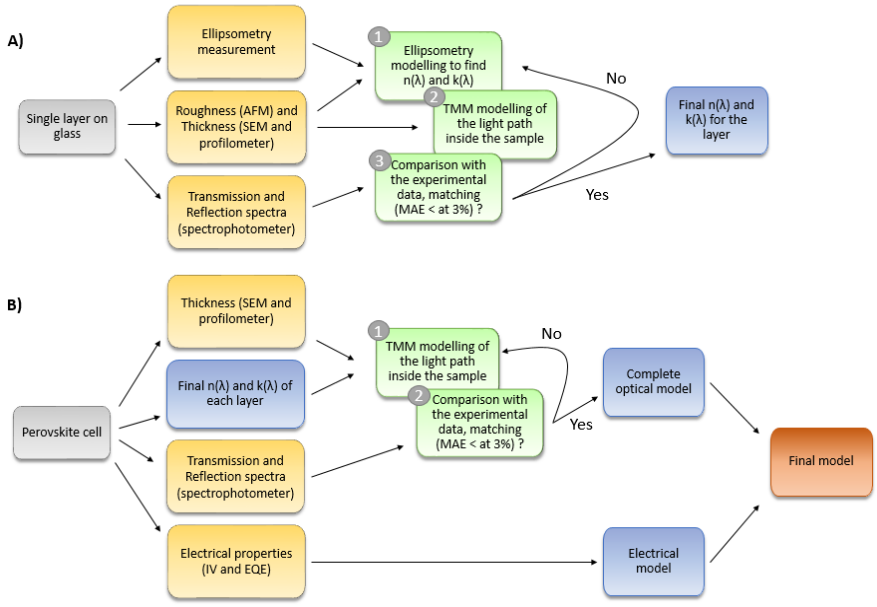

Fig. 2. The process with two steps used to find the optical indices with the iteration cycle and the final model: A) layer deposited on glass and B) complete perovskite solar cell

Table I. Dispersion models used to fit the optical indices in ellipsometry measurements for each material, and value of the least square error coefficient X^2.

Sample	Models of dispersion	X^2
Glass (TEC7)	Herzberger	0.1
SnO_2 (TEC7)	Lorentz oscillator	1.4
SiO_2 (TEC7)	Lorentz oscillator	1.4
FTO (TEC7)	New Amorphous + Drude	3.9
Compact TiO_2	Lorentz oscillator	4.4
Mesoporous TiO_2	Lorentz oscillator	2.3
Perovskite	5x Tauc Lorentz + Lorentz oscillator	1.4
Spiro	4x Tauc Lorentz + Lorentz oscillator	1.7
ITO	New amorphous + Drude	13.1

Table II. MAE between the fitted model and the experimental data for transmission (T), reflection (R) and absorption (A), for layer on glass and the semitransparent perovskite cell.

Cell	T (%)	R (%)	A (%)
Glass	0.99	1.08	1.50
TEC7 without FTO	1.87	2.02	1.96
TEC7 with FTO	2.33	1.58	2.43
Compact TiO_2	1.35	2.42	1.89
Mesoporous TiO_2	2.74	1.28	0.99
Perovskite	2.05	2.29	2.98
Spiro	1.60	1.82	1.19
ITO	2.14	2.44	1.61
Semi-transparent perovskite cell	1.19	1.21	1.12

3.2 The soda-lime glass substrate modeled as an incoherent layer

To model the TEC7 substrate, the analysis is performed in three steps: the glass alone, the "etched" TEC7 and the complete substrate stack. For the soda-lime glass alone, transmission measurements revealed residual absorption. We used the optical indices given by Rubin [22], based on simplified form of the dispersion equations from Herzberger [23].

Conventional TMM codes simulation of thick transparent substrates considers planar interfaces inducing interferences that due to the light reflection at both planar interfaces. However, the bottom and top surfaces of glass substrates are not perfectly flat and parallel and such oscillations are not visible in their optical response. In addition, the coherence length of the light is much shorter than the thickness of the glass, which causes a complete disappearance of the interference patterns. To account for this behavior, thick glass layers can be modeled as incoherent layers in the TMM code by following Troparevsky et al. [24]. The propagation matrix L_j of an incoherent layer j placed anywhere in the stack is calculated by adding a random phase ξ:

$$L_j = \begin{bmatrix} e^{-i\left(\frac{2\pi n_j t_j}{\lambda}+\beta.\xi\right)} & 0 \\ 0 & e^{i\left(\frac{2\pi n_j t_j}{\lambda}+\beta.\xi\right)} \end{bmatrix} \qquad (2)$$

with t_j the thickness of the layer j, n_j the complex refractive index of the layer j, λ the wavelength and ξ a random number between -1 and 1. If $\beta = 0$, the phase is not randomized, the layer simulated is coherent. In the following, we choose $\beta = \pi$ to simulate a completely random phase in the incoherent glass substrate.

With this solution, the TMM code has been run with different ξ values, and the results have been averaged to eliminate the random variation of the phase and interference effects. 50 iterations are required to accurately smooth the modeled optical response as shown in Fig.3. Alternatively, the approach proposed by Santbergen et al could considered for further improvements in cases where the calculation time would become too long [25].

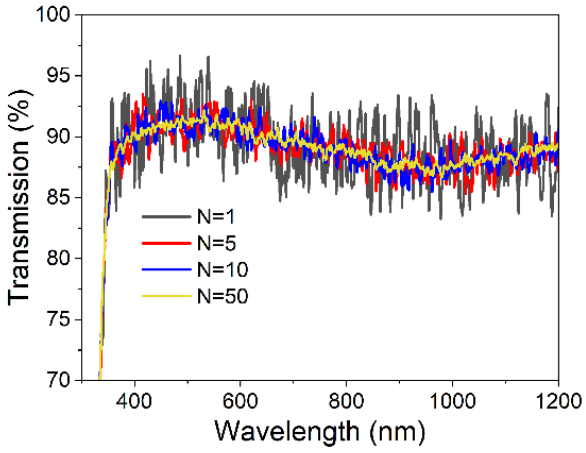

Fig. 3. Simulated transmission spectra of soda-lime glass using random phases to smooth interference effects, as function of the number of iterations *N*.

3.3 Complete substrate stack

Usually the commercially available FTO covered glasses include the presence of a SiO_2 / SnO_2 bilayer between glass and the TCO layer [9,10]. The thin film of SnO_2 is used to increase the hardness of the glass and facilitates the adhesion of SiO_2. Then the SiO_2 layer acts as diffusion barrier of alkali oxides from the glass into the upper layers. These layers must be taken into account for the optical modeling even if they have no electrical role in the structure, just like the substrate. The "etched TEC7" substrate was successfully modeled described considering 9 nm of SnO_2 and 30 nm of SiO_2, leading to a least square error coefficient X^2 of 1.4. The indices of these two materials are modeled with a single Lorentz oscillator. For the FTO layer itself, another dispersion model is considered, due to its wide bandgap of 3.8 eV and its free-carrier absorption in the infrared region. The new amorphous dispersion model (NAM), develop by Horiba and based on the Forouhi-bloomer formulation [26,27], is used for the absorption in UV range and the Drude model is used for the absorption in the infrared region. The fit of the complete substrate Glass / SnO_2 / SiO_2 / FTO gives slightly degraded but still satisfying square error X^2 of 3.9 for such a complex stack with 4 different layers. The higher value of X^2 compared to the TEC7 etched stack originates from the presence of the additional FTO layer and can be attributed to the roughness of the FTO layer (RMS=11.73 nm, see Fig.4.A), not considered in our models. This assumption is confirmed by the comparison between experimental and simulated reflection and transmission spectra plotted in Fig.4.B, where the fringes at short wavelengths are attenuated in experimental spectra. For the sake of simplicity, we stay with a model with no roughness effect, and we obtain a good overall agreement (MAE of less than 3%).

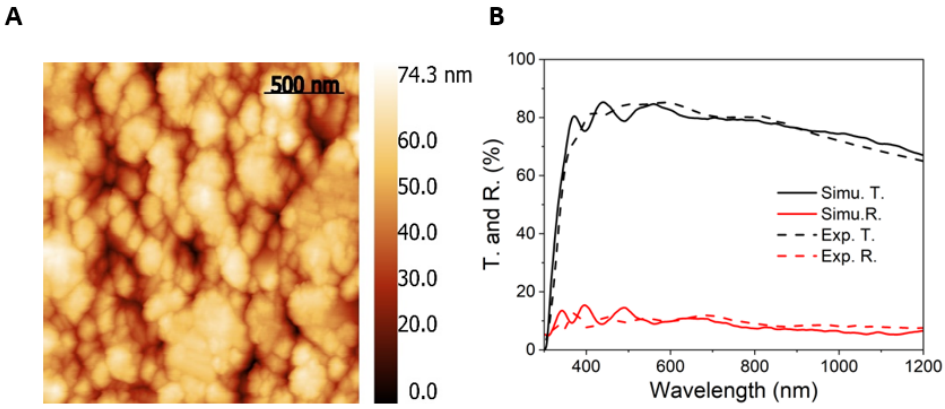

Fig. 4. A. AFM measurement of the FTO surface. B. Simulated and experimental spectra of reflection and transmission for TEC7 substrate.

3.4 ITO electrode modeling

The same dispersion model is used for ITO as for FTO (NAM and Drude). In this case X^2 is higher than that of other films, therefore (13.1). This can be explained by the variation of the crystalline properties of this layer as a function of its thickness. Thus, ITO is deposited at room temperature to avoid the damage on the Spiro-OMeTAD layer. In these soft growth conditions, the ITO layer has been shown to evolve from amorphous to polycrystalline for thickness higher than 200 nm [28–31]. Thus, in our case, with a thickness of 280 nm and a sheet resistance of 17.5 Ω.sq, the film may be no longer homogeneous in depth, with a material potentially amorphous near the substrate and polycrystalline close to the surface. Since the degree of crystallization of a material impact its optical properties, the refractive indices average the contributions of the different crystalline states present in the actual layer. Fig. 5 shows the optical index *n* and *k* of different ITO layers deposited in the same conditions but with different

deposition times in to vary the thickness. The sheet resistance decreases from 29 Ω.sq for a thickness of 180 nm to 17 Ω.sq for a thickness of 270 , and then is constant for thicknesses up to 470 nm (16 Ω.sq), see Fig. S3. In parallel extinction coefficient k continues to increase in the infrared when the thickness of the ITO layer increases.

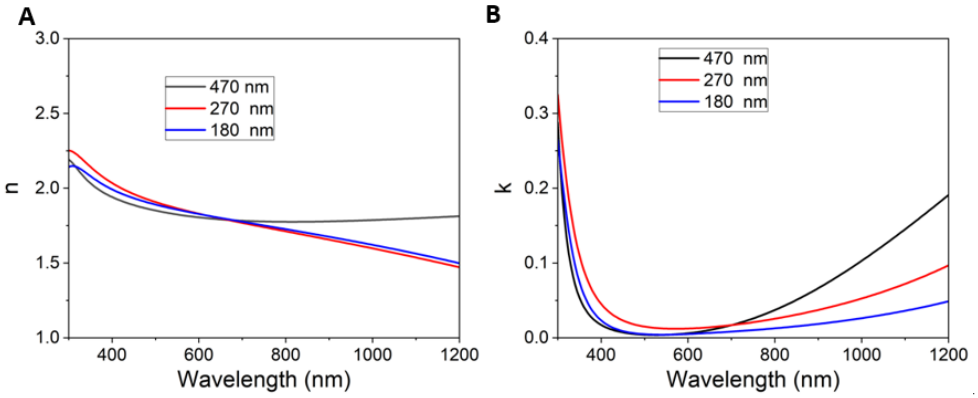

Fig. 5. A. Refractive index and B. Extinction coefficient *k* of ITO layers with different thicknesses.

3.5 Spiro-OMeTAD and Perovskite layers modeling

Spiro-OMeTAD and perovskite have been poorly characterized by ellipsometry in the literature, and their optical characteristics vary as function of material compositions and preparation method condition, as shown in Fig.6 for the perovskite [32]. In addition, different dispersion models and fitting method can be used for these materials as their optical index show different peaks that cannot be fit with single oscillator. Here, the Tauc Lorentz model [33] is implemented for both Spiro-OMeTAD and perovskite materials. It describes the electronic transition parameters such as the optical band gap and the peak transition energy that can be found in the typical continuum of band absorption of these materials. For example, concerning the perovskite, the three peaks observed at 400 nm, 516 nm and 754 nm, correspond to optical transition energies [34] and are attributed to direct semiconductor-type transitions at the X, M, and R points in the pseudo-cubic Brillouin zone, respectively [35,36].

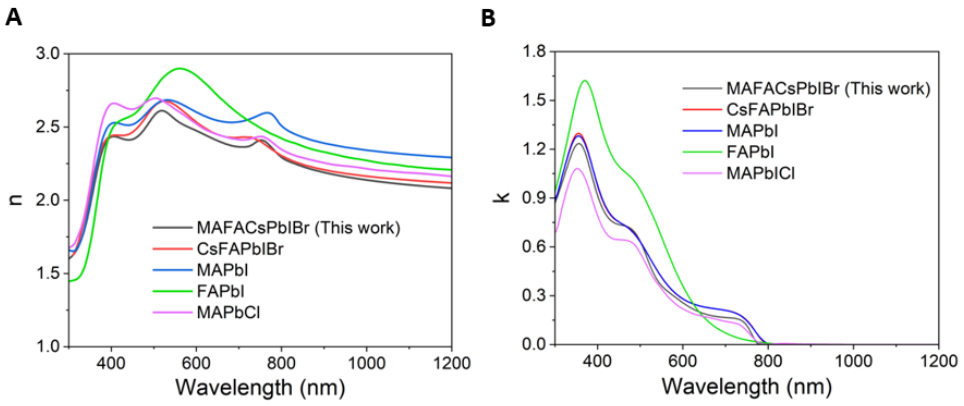

Fig. 6. A. Refractive index n and B. extinction coefficient k for different perovskite composition: MAFACsPbIBr of this work, CsFAPbIBr [11], MAPbI [12], FAPbI [18] and MAPbCl [13].

Nevertheless, Spiro-OMeTAD and perovskite layers deposited on glass are different from the layers in the complete stack. In particular, both the thickness and roughness of the spin-coated layers depend on the underlayer. In order to obtain reliable optical indices, the thickness and roughness of layers are first measured on glass, and then in the complete stack using the SEM cross-section shown in Fig.1.A.

3.6 TiO_2 Bilayer modeling

A single Lorentz oscillator is also used for the refractive indices of the mesoporous and compact TiO_2 layers, as the SnO_2 and SiO_2 layers, as it adequate to model semiconductors.

The mesoporous TiO_2 is described by the following structure which allows to obtain after several iterations the lowest X^2 equal to 2.3: a layer made of 50% of TiO_2 and 50% of air (22 nm) is placed between two layers which contain 25% of TiO_2 and 75% of air (90 and 44 nm) to take into account the fact that the air and the mesoporous TiO_2 are mixed during this step of determination of the optical indices. The final optical indices of this TiO_2 material are, however, combined with those of the perovskite and not of the air, since the mesoporous TiO_2 layer is filled by perovskite in the complete semitransparent cell, as evidenced by scanning transmission electron microscopy analyses. This stack follows AFM observations (Fig. 7.A) which shows thickness variations of 107 nm while the layer is between 100 and 120 nm thick, and was required to fit the transmission and reflection spectra, see Fig.7.B.

Another solution has been tested to simulate the optical behavior of the mesoporous layer by modeling the roughness of its bottom and top interfaces. A roughness factor is implemented in the refraction matrix of a rough interface between two layers *i* and *j* as suggested by Szczyrbowski [37,38] :

$$I_{i\to j} = \begin{bmatrix} 1 & r'_{ij} \\ r'_{ij} & 1 \end{bmatrix} * \frac{1}{t'_{ij}} \qquad (3)$$

$$\text{with } r'_{ij} = \frac{n_i - n_j}{n_i + n_j} * e^{-2*(\frac{2\pi n_2 \sigma}{\lambda})^2} \text{ and } t'_{ij} = \frac{2*n_i}{n_i + n_j} * e^{-\left(\frac{2\pi\sigma}{\lambda}\right)^2 * \frac{(n_j - n_i)^2}{2}}$$

where n_i and n_j are the complex refractive indices of the layers, r'_{ij} and t'_{ij} the reflection and transmission Fresnel coefficients of the interface, and σ the roughness factor. The surface is flat when $\sigma = 0$. As show in Fig.7.B, the best fit of the experimental data is obtained with this second model and $\sigma = 200$, in particular between 300 and 600 nm.

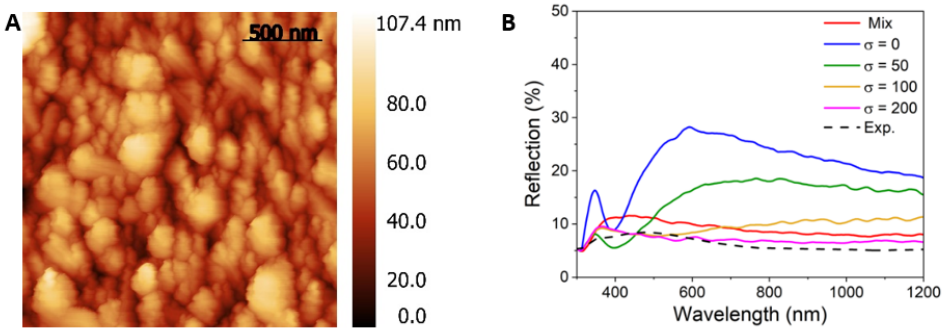

Fig. 7. A. AFM measurement of the mesoporous TiO_2 surface. B. Experimental and simulated spectra of reflection with a "mixed" layer (TiO_2 / Air) or with roughness factor σ for mesoporous TiO_2 on glass.

In parallel, the compact TiO_2 is modeled as a single layer of 40 nm, leading to a least square error coefficient X^2 of 4.4. The same optical indices cannot be used for compact and mesoporous TiO_2 because they have different bandgap. As these two materials are not deposited by the same method (Spin-coating vs. spray) and by the same solution, chemical differences are likely to exist (contamination or oxygen deficiency).

4. Modeling the complete solar cell

4.1 Optical model

The final indices n and k obtained for each layer after the iterative method are presented in Fig.8. A and B, respectively. The indices obtained without the iterative method are presented in Fig. S5. Differences can be observed for all layers. In the case of perovskite, the intensities of the peaks of the optical transition energies for the indices n and k present strong variations. Another striking example is ITO, whose index n has a different behavior in the IR which will lead to different properties of reflection.

The second step B of the iterating process described in Fig.2.B is carried out to model the optical properties of the complete solar cell. The cell is in a superstrate configuration and modeled as illuminated through the glass first. Using the TMM, absorption, transmission, and reflection spectra of the semitransparent perovskite solar cell without front contact grid are simulated and compared with experimental data in Fig.9. A very good agreement is obtained, with MAE around 2% in each case (see Table III). The bandgap of the perovskite absorber is E_g=1.58 eV, corresponding to a wavelength of 785 nm. If the incident photons are fully absorbed for wavelengths below 500 nm, a slow increase of optical transmission is observed between 500 nm to 750 nm. This behavior that is usually described in the literature is related to the thickness of the perovskite layer that remains too thin to absorb all the incident light in this range (650 nm). Beyond the perovskite bandgap wavelength, transmission reaches a maximum of 72% at 820 nm, and decreases until 1200 nm at 52%. The total reflection is constant and below 10% over the whole spectral range, except between 800 and 1000 nm where interference fringes appear and are responsible for a reflection maximum of about 17% at 900 nm. Additional interference fringes are observed in transmission spectra that are well described by the simulation. Finally, an unexpectedly high absorption is observed above 800 nm, rising from 20% to 40% at 1200 nm.

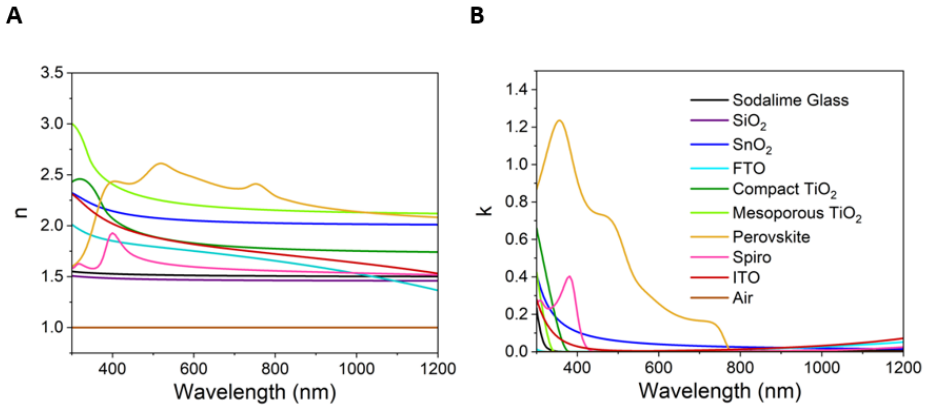

Fig. 8. A. Final optical indices *n* for each layer. B. Final optical indices *k* for each layer.

In order to better evidence the influence of the iterative method on MAE, the simulated spectra are compared with results obtained using optical indices published in the literature and determined using our experimental data without the iterative method, see Fig. 9. The stack and the thicknesses of each layer are similar for the 3 simulations and only the optical indices and the interface roughness change. The total absorption fits approximately the experimental data when the iterative method is not used (MAE =2.69%), but the transmission spectra (Fig. 9 B) show that only the simulation using the iterative method allows to correctly fit the interference figures in the range 800 nm – 1200 nm. This is reflected in the MAE values, which remain above 3% when the iterative method is not used, see Table III. Looking in detail at the simulations obtained without iterative methods on each individual layer in Fig S3, a similar phenomenon is observed. In particular, TiO_2 layers show transmission and reflection spectra far from the experimental measurements, and the TEC7 substrate features important interferences in transmission spectra. The use of unsuitable indices leads to a poor evaluation of the different phenomena of reflection and transmission in individual layers, which is reflected in the interference figures observed on the complete stack.

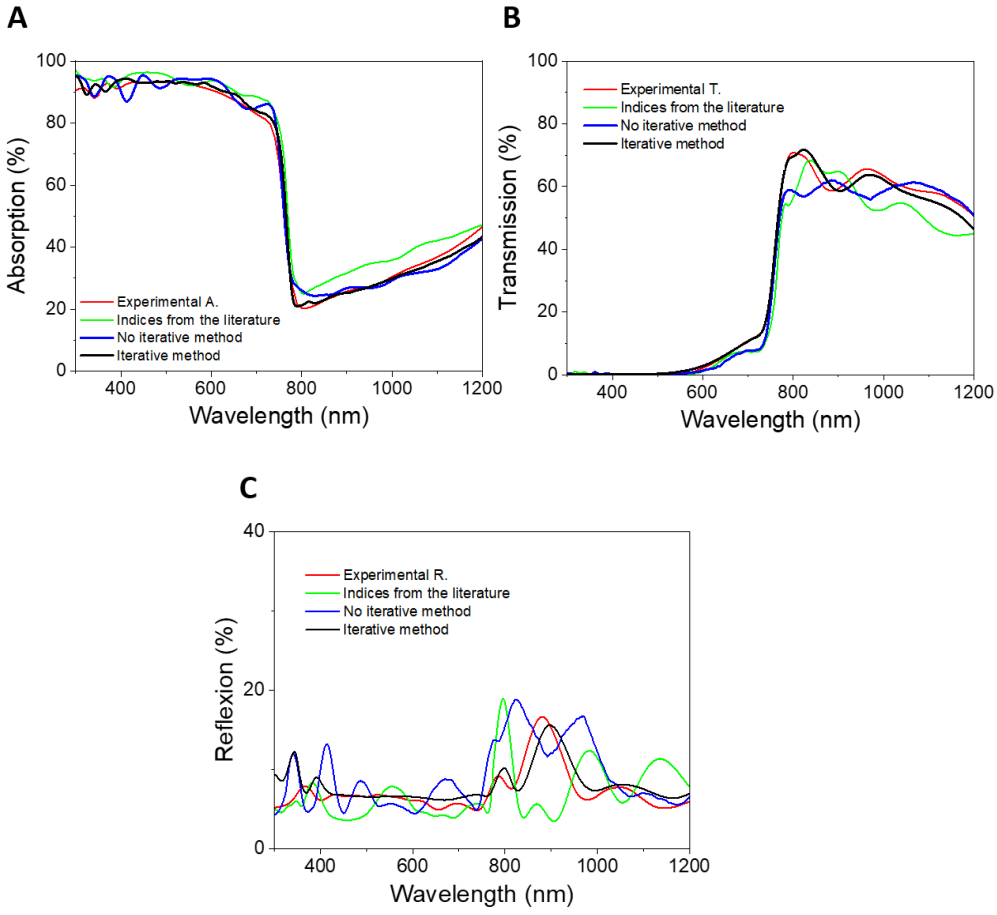

Fig. 9. Experimental and simulated spectra for A) absorption, B) transmission and C) reflection of the semitransparent perovskite solar cell stack using indices from the literature (as close as possible to our materials) and using fits of our experimental data with or without the iterative method.

Table III. MAE between experimental and simulated absorption, transmission and reflection spectra of the semitransparent perovskite solar cell stack with indices from the literature, and from experiments fitted with or without the iterative method.

Cell	T (%)	R (%)	A (%)
Iterative method	1.19	1.21	1.12
No iterative method	2.57	4.20	2.69
Indices of literature	4.59	3.14	4.21

Simulation by TMM allows to separately quantify the absorption in each single layer of the structure, and to reveal the origin of the main losses, as shown in Fig.10.A. The main parasitic absorption occurs in the infrared region and can be attributed to free-carrier absorption in the TCO. The FTO electrode is the most problematic layer absorbing 15% of incident light at 1000 nm. At this wavelength, the second top ITO electrode also absorbs 7.3%, the soda-lime glass 5.2% and the Spiro-OMeTAD 2.5%. In the visible between 400 nm and 800 nm, the absorption in the perovskite layer is limited by the one of the FTO (5.2% at 600 nm). Similarly, Fig.10. B and C present the simulated absorption of each layer using indices published in the literature and fitted from experiments without the iterative method. Table IV gives the absorption values of the different layers at 400 and 1200 nm for each simulation. Although the total absorption simulated with these two models presented in Fig.9.A seems accurate compared to the experimental spectrum, its decomposition in every layer shows marked differences between the 3 models. Fig. 10 and Table III exhibit striking differences in the parasitic absorption in TCO layers (FTO, ITO and TiO_2) at short (400 nm) and long (1100 nm) wavelengths. Overall, the iterative method leads to more balanced parasitic absorption between these TCO layers, and a significantly higher absorption efficiency in the perovskite layer. The accuracy of the model is of high importance to further improve semi-transparent perovskite solar cells for tandem devices.

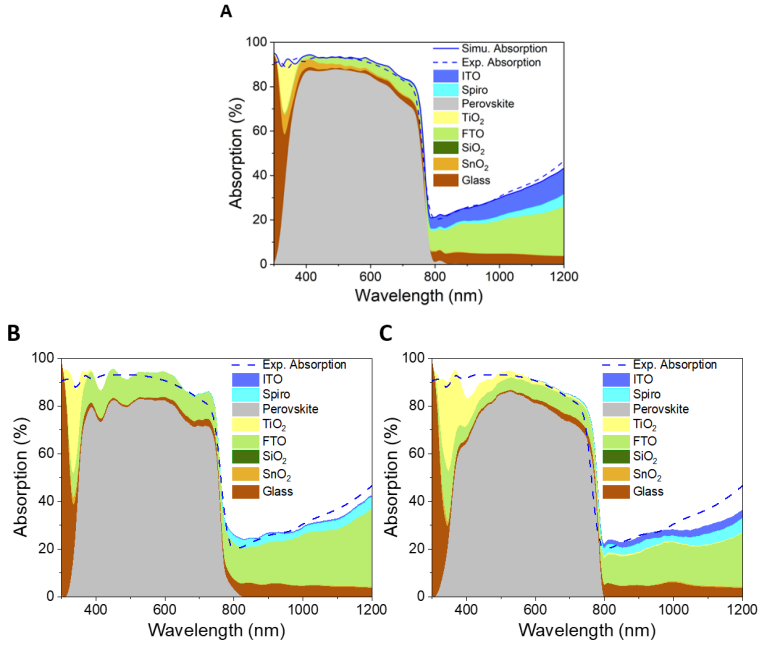

Fig. 10. A. Simulated (blue curve) and experimental (blue dashed curve) total absorption of the perovskite cell and simulated absorption into each layer of the semitransparent perovskite solar cell stack using our experimental data A. with or B. without the iterative method, and C. using indices from the literature (as close as possible to our materials)

Table IV. Simulated absorption into each layer of the semitransparent perovskite solar cell stack using our experimental data with or without the iterative method and using indices from the literature.

	Iterative method		No iterative method		Indices of literature	
Layers	A. at 400 nm (%)	A. at 1100 nm (%)	A. at 400 nm (%)	A. at 1100 nm (%)	A. at 400 nm (%)	A. at 1100 nm (%)
Glass (TEC7)	1.55	4.1	1.5	4.08	1.69	4.03
SnO_2 (TEC7)	3.87	0.24	0.06	0.32	0.07	0.34
SiO_2 (TEC7)	0	0	0	0	0	0
FTO (TEC7)	2.05	17.82	12.24	23.88	5.31	17.43
TiO_2	0	0	0.22	0	11.74	0.29
Perovskite	86.59	0	75.8	0	64.51	0
Spiro	0	3.44	0	3.96	0	4.78
ITO	0	9.84	0	0.62	0	3.52

Total reflection is also responsible for significant optical losses. These last are analyzed by simulating gradually the reflection of the different parts of the whole stack starting from the first air / glass interface and successively adding each layer of the perovskite solar cell stack one after the other. Thus, the reflection at the ITO / air interface considers the contribution of the whole stack and the reflections at the other interfaces. Each reflection intensity is defined as the square module of the reflection coefficient r_j on the stack made of the layers 1 to j-1, including the interface between the layer j-1 and a semi-infinite layer j. It is derived from the TMM:

$$R_j = |r_j|^2 = \left|\frac{S'_{j2,1}}{S'_{j1,1}}\right|^2 \text{ and } S'_j = \begin{bmatrix} S'_{j1,1} & S'_{j1,2} \\ S'_{j2,1} & S'_{j2,2} \end{bmatrix} = \left(\prod_{v=1}^{j-1} I_{(v-1)v} L_v\right). I_{(j-1)/j} \qquad (4)$$

with I_n the refraction matrix, L_n the phase matrix and S_j' the partial transfer matrix of the system including the first layer until the layer j-1.

Fig. 11 shows that the main interference patterns visible in the total reflection spectrum at 780 nm and 880 nm are due to two different interfaces: the perovskite / spiro-OMeTAD one, which firstly generates two peaks up to 7.1% and 9.2%, and the ITO / air interface, which further increases the reflection maxima up to 9.5% and 17.2%, respectively. This is caused by the high difference between the refractive indices of the couples perovskite / spiro-OMeTAD, and ITO / air at 900 nm (2.19 – 1.55 and 1.67 – 1 respectively). This is also the case for the SnO_2 / SiO_2 interface but due to the very low thickness of the SiO_2 film, a large part of the evanescent wave generated at the interface reaches the rear face and spreads into the stack without generating reflection. The first air / glass interface is also responsible for a non-negligible reflection of 4.4% over the entire spectrum. Finally, a small interference pattern is also visible at 360 nm (reflection maximum of 7.1%) and it is related to the FTO / compact TiO_2 interface.

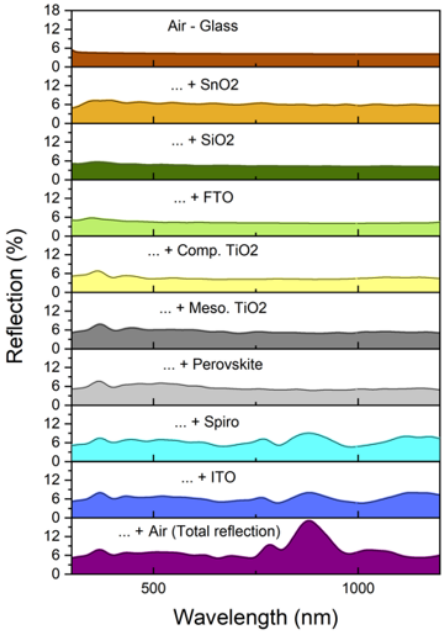

Fig. 11. Reflection generated at each interface of the perovskite cell. The spectrum for the ITO-air interface corresponds to the total reflection on Fig.9.C.

4.2 Electrical model

4.2.1 Theoretical modelling details

The optical and electrical performances of the tandem solar cell are intrinsically linked because it is always a question of finding a compromise between transparency and conductivity. Indeed, the power generated in the silicon cell depends on the optical transmission through the perovskite stack, and particularly on the transparency of TCO layers. Then the optical and electrical properties of the TCO layers must be carefully balanced to optimize the whole tandem cell. In the following, we propose a simple electrical model to predict the performances of a 4T tandem device when the perovskite stack is tuned compared to the experimental reference structure presented here.

Firstly, the internal quantum efficiency (IQE) of the perovskite cell is defined using the ration between the experimental EQE ($EQE_{xp-pero1}$) and the simulated absorption ($A_{simu-pero1}$):

$$IQE_{pero}(\lambda) = \frac{EQE_{exp-pero\,1}(\lambda)}{A_{simu-pero\,1}(\lambda)} \quad (5)$$

with $EQE_{xp-pero1}$ is the measured external quantum efficiency of the experimental perovskite cell and $A_{simu-pero1}$ is the simulated absorption of the perovskite layer in the reference stack. IQE_{pero} is close of 90% in the entire spectra and then is used to predict the EQE for the perovskite cell for optically different structures:

$$EQE_{simu-pero}(\lambda) = IQE_{pero}(\lambda) * A_{simu-pero\,2}(\lambda) \quad (6)$$

with $A_{simu\text{-}pero2}$ is the simulated absorption of the perovskite layer in the new stack. For the silicon solar cell, we define the normalized EQE_{Norm} as:

$$EQE_{Norm}(\lambda) = \frac{EQE_{exp-si}(\lambda)}{T_{exp}(\lambda)} \quad (7)$$

With T_{exp} the measured transmission of the experimental perovskite cell and $EQE_{exp\text{-}si}$ the measured external quantum efficiency of the silicon cell. The EQE predicted for a silicon cell filtered by T_{simu} is given by:

$$EQE_{simu-Si}(\lambda) = EQE_{Norm}(\lambda) * T_{simu}(\lambda) \quad (8)$$

With T_{simu} the simulated transmission of the perovskite cell. If the perovskite solar cell architecture is modified with no change of the active layers (absorber and TiO_2 / spiro-OMeTAD selective contacts), IQE_{pero} and EQE_{Norm} can be considered as unchanged to evaluate the performances of the resulting tandem cell.

The simulated electrical characteristics of both perovskite and silicon cells ($J_{sc\text{-}simu}$ and $V_{oc\text{-}simu}$) are derived as follows [36]:

$$J_{sc-simu} = -q \int_{\lambda_2}^{\lambda_1} EQE_{simu}(\lambda)\phi(\lambda)d\lambda \quad (9)$$

$$V_{oc-simu} = ln\left(\frac{J_{sc-simu}}{J_{sc-exp}}\right) * \frac{mk_bT}{q} + V_{oc-exp} \quad (10)$$

with EQE_{simu} the simulated EQE of the cells, m the ideality factor, $J_{sc\text{-}exp}$ and $V_{oc\text{-}exp}$ the experimental electrical characteristics of the reference cells.

In the semitransparent perovskite solar cell, the FF is strongly affected by the sheet resistance of TCOs. Thus, FF can be divided into two contributions: (1) losses due to the sheet resistance of the TCOs and (2) the other contributions. In the case of our experimental devices, the contact design is asymmetrical. The two TCOs are made of two different materials, do not have the same conductivity and geometrically, the current does not travel the same distance inside. This results in different equations for the front and back electrodes. The power loss P_{TCO} due to the sheet resistance of the rear (ITO) and the front (FTO) TCO electrodes can be calculated as follows [40]:

$$P_{TCO-rear} = \int I^2 y \, dR = 2\int_0^{D/2} (JLy)^2 \frac{R_{sh-rear}}{L} \, dy = \frac{J^2 L D^3 R_{sh-rear}}{12} \quad (11)$$

$$P_{TCO-front} = \int I^2 y \, dR = \int_0^{d} (JLy)^2 \frac{R_{sh-front}}{L} \, dy = \frac{J^2 L d^3 R_{sh-front}}{3} \quad (12)$$

with D the distance between the gold contact and the center of the rear electrode and d the distance between the gold contact and the center of the front electrode, see Fig.12.C, L the finger length, R_{sh} the sheet resistance of the TCO, y the distance between a gold contact and a point of the TCO surface, I the current and J the current density. Afterwards, P_{TCO} is normalized by the power estimated at the maximum power point (P_{MPP}) to find the losses X due to the sheet resistance of one TCO:

$$\chi_{TCO-rear} = \frac{P_{TCO-rear}}{P_{MPP}} = \frac{R_{sh} * D^2}{12} * \frac{J_{MPP}}{V_{MPP}} \quad (13)$$

$$\chi_{TCO-front} = \frac{P_{TCO-front}}{P_{MPP}} = \frac{R_{sh}*d^2}{3} * \frac{J_{MPP}}{V_{MPP}} \quad (14)$$

with J_{MPP} and V_{MPP} the current and voltage at the maximum power point, respectively. Finally, the efficiency of the cell can be estimated by:

$$PCE_{simu} = \frac{1}{P_i} * J_{sc-simu} * V_{oc-simu} * FF$$
$$with\ FF = FF_0 - \mathrm{X}_{TCO-rear} - \mathrm{X}_{TCO-front} \quad (15)$$

with P_i the incident light power and FF_0 is the FF without electrical losses in the electrodes.

4.2.2 Experimental results

The experimental perovskite top cell used to develop this optical model reached 16.6% efficiency and allowed to build a 4T tandem at 21.7% of efficiency by associating it to a filtered commercial silicon bottom cell at 5.1% [8]. This device suffers from electrical and optical losses and constitutes an interesting starting point to validate our model. Once the main losses are identified, different pathways are proposed to simultaneously optimize the performances of both perovskite and silicon subcells. For that purpose, the experimental electrical performances of the perovskite, silicon solar cells and filtered silicon cells have been obtained with the I-V characteristic under one-sun AM1.5G illumination. The results are given in Table III and in Fig.12.A.

The IV curve of the experimental perovskite cell is fitted with a diode model to obtain the value of the ideality factor m, i.e. m=3.3. While the ideality factor is generally between 1 and 2, higher ideality factor can be observed in perovskite cell, and it is due to the presence of strong coupling between ions and electrons near the electrode interface. A presence of such interfacial defects are known to give an abnormally large ideality factor for organic photovoltaic cells [41,42]. For the silicon cell, we consider m=1. As visible on Fig.12.B, simulated EQE for the silicon cell has a slight discrepancy with the experimental measurement, with no impact on the Jsc because losses and gains offset each other. EQE is mainly limited by the transmission through TCO at the front side and the rear side of the perovskite cell.

In the case of the perovskite device, the losses are also due to the sheet resistance of TCO. Losses due to sheet resistance can be obtained using d is 8 mm for the anode (FTO) and D is 3 mm for the cathode (ITO), see diagram in Fig.12.C and D. Consequently, XTCO-rear loss is equal to -4.58% and XTCO-front loss is equal to -0.28% following the equations (13) and (14), respectively. Consequently, by using equation (15), FF0 is equal to 78% to obtain the same fill factor and efficiency as experimentally measured, see Table III. In interesting to note that, according to the Shockley-Queisser model, the upper limit of FF is close to 90% for perovskite solar cells with open circuit voltages of 1.2V and an idealized factor m=1. This first percentage of loss (10%) is due to radiative recombination which is an unavoidable loss mechanism. However, in many cases as here, the maximum reachable FF to about 83% [43]. In such devices, it is then mainly limited by non-radiative recombination losses. In addition, best practical devices have generally lower FF (around 70-75%). The presence of defects in the absorber material, inefficient charge extraction or current leakage through shunts can already limit the achievable FF below the maximum value, even in the absence of resistance effects in the electrodes or other layers [43,44]. That shows the good quality of the perovskite solar cell used in this work regardless the electrodes.

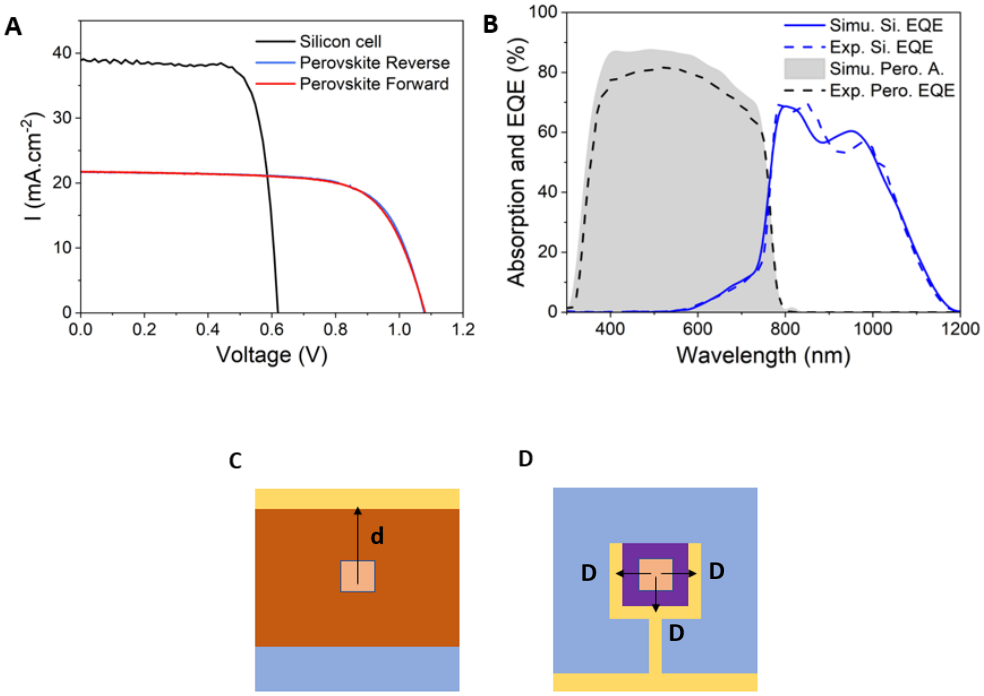

Fig. 12. A. IV curves of the semitransparent perovskite cell under 1-sun illumination and the unfiltered silicon cell. B. Simulated (blue curve) and experimental (blue dash curve) filtered silicon EQE and simulated absorption (grey area) and experimental EQE (black dash curve) of the semitransparent perovskite cell. Schematic representation of C. the front side of the perovskite device (Glass/FTO) and D. the back side (ITO/Air). The yellow bars represent the gold electrodes, the brown rectangle the FTO coated surface and the purple square the ITO electrode. The central orange square represents the illuminated area of the sample constituting the 0.09 cm^2 perovskite cell.

Table V. Electrical characteristics of the perovskite and silicon solar cells under one-sun AM1.5G illumination, and of the filtered silicon cell.

Cell	Eff. (%)	Jsc ($mA.cm^2$)	Voc (mV)	FF (%)
Perovskite	16.6	21.1	1075	73
Silicon	18.1	38.9	619	77
Filtered Silicon	5.1	11.5	590	77
Tandem	21.7	-	-	-

5. Conclusion

In conclusion, we developed an optical model and an iterative methodology to simulate accurately an experimental perovskite cell, and a 4T perovskite/silicon tandem device. It is based on an iterative method: the determination of the optical indices of every layer of the structure, and the model of the complete structure. Optical losses in the perovskite cell have been analyzed. Parasitic infrared absorptions are mainly caused by the electrodes (ITO and FTO), spiro-OMeTAD and the glass substrate. Furthermore, the air / glass and ITO / air interfaces are responsible of parasitic reflection.

In addition, to predict the impact of changes in the initial structure, for instance new TCO layers, we developed a simple electrical model to simulate the full tandem cell. In our design, FTO is the main factor limiting the FF of the perovskite cell, even if its sheet resistance is lower than ITO.f

Our models can be used to further improve the efficiency of the 4T tandem solar cells. It provides a simple way to test many materials in order to optimize the complete device, for instance by replacing Spiro by PTAA, or using IZO and IO:H for the electrodes. Parasitic reflection could be reduced by the use of additional anti-reflective coatings, and by adding an optical coupling layer between the cells. Finally, the interest of using more efficient bottom silicon cells from different technologies can be easily evaluated thanks to the electrical model mentioned.

More generally, the methodology detailed here can be easily applied to other technologies of solar cells and allow building optical models based on experimental devices when the morphology, the optical, and electrical properties can be characterized. It can accound for a wide variety of materials and stacks, and oblique incidence angles. In addition to the analysis of optical losses, the ability to finely model interference patterns may be of particular interest in structures where their influence on transmission and reflection properties needs to be enhanced/suppressed for optical management.

Acknowledgments. This project is supported at IPVF by the French Government in the frame of Programme d'Investissement d'Avenir – ANR-IEED-002-01.

Disclosures. The authors declare no conflicts of interest.

Data availability. Data underlying the results presented in Figure 8.A and B are available in Dataset 1.

Supplemental document. See Supplement Document 1 for: 1. Simplified diagram of the evolution of X^2 and MAE as a function of the number of iterations, 2. Ellipsometry models and fits, 3. Simulated and experimental transmission, reflection and absorption spectra for each layer, 4. Evolution of the thickness of the sheet resistance of standard ITO deposited on glass as a function of the deposition time and 5. Optical indices when iterative method is not used.

References

1. A. Richter, M. Hermle, and S. W. Glunz, "Reassessment of the Limiting Efficiency for Crystalline Silicon Solar Cells," IEEE J. Photovolt. **3**, 1184–1191 (2013).
2. R. M. Swanson, "A vision for crystalline silicon photovoltaics," Prog. Photovolt. Res. Appl. **14**, 443–453 (2006).
3. A. Kojima, K. Teshima, Y. Shirai, and T. Miyasaka, "Organometal Halide Perovskites as Visible-Light Sensitizers for Photovoltaic Cells," J. Am. Chem. Soc. **131**, 6050–6051 (2009).
4. "National Renewable Energy Laboratory (NREL)," https://www.nrel.gov/.
5. B. Chen, X. Zheng, Y. Bai, N. P. Padture, and J. Huang, "Progress in Tandem Solar Cells Based on Hybrid Organic–Inorganic Perovskites," Adv. Energy Mater. **7**, 1602400 (2017).
6. J. Werner, B. Niesen, and C. Ballif, "Perovskite/Silicon Tandem Solar Cells: Marriage of Convenience or True Love Story? – An Overview," Adv. Mater. Interfaces **5**, 1700731 (2018).
7. N. N. Lal, Y. Dkhissi, W. Li, Q. Hou, Y.-B. Cheng, and U. Bach, "Perovskite Tandem Solar Cells," Adv. Energy Mater. **7**, 1602761 (2017).
8. F. J. Ramos, S. Jutteau, J. Posada, A. Bercegol, A. Rebai, T. Guillemot, R. Bodeux, N. Schneider, N. Loones, D. Ory, C. Broussillou, G. Goaer, L. Lombez, and J. Rousset, "Highly efficient MoOx-free semitransparent perovskite cell for 4 T tandem application improving the efficiency of commercially-available Al-BSF silicon," Sci. Rep. **8**, 16139. (2018).
9. J. M. Ball, S. D. Stranks, M. T. Hörantner, S. Hüttner, W. Zhang, E. J. W. Crossland, I. Ramirez, M. Riede, M. B. Johnston, R. H. Friend, and H. J. Snaith, "Optical properties and limiting photocurrent of thin-film perovskite solar cells," Energy Environ. Sci. **8**, 602–609 (2015).
10. Y. Jiang, I. Almansouri, S. Huang, T. Young, Y. Li, Y. Peng, Q. Hou, L. Spiccia, U. Bach, Y.-B. Cheng, M. A. Green, and A. Ho-Baillie, "Optical analysis of perovskite/silicon tandem solar cells," J. Mater. Chem. C **4**, 5679–5689 (2016).
11. J. Werner, G. Nogay, F. Sahli, T. C.-J. Yang, M. Bräuninger, G. Christmann, A. Walter, B. A. Kamino, P. Fiala, P. Löper, S. Nicolay, Q. Jeangros, B. Niesen, and C. Ballif, "Complex Refractive Indices of Cesium–Formamidinium-Based Mixed-Halide Perovskites with Optical Band Gaps from 1.5 to 1.8 eV," ACS Energy Lett. **3**, 742–747 (2018).

12. S. Manzoor, J. Häusele, K. A. Bush, A. F. Palmstrom, J. Carpenter, Z. J. Yu, S. F. Bent, M. D. Mcgehee, and Z. C. Holman, "Optical modeling of wide-bandgap perovskite and perovskite/silicon tandem solar cells using complex refractive indices for arbitrary-bandgap perovskite absorbers," Opt. Express **26**, 27441 (2018).
13. Y. Jiang, M. A. Green, R. Sheng, and A. Ho-Baillie, "Optical modelling data for room temperature optical properties of organic–inorganic lead halide perovskites," Data Brief **3**, 201–208 (2015).
14. M. Zhao, Y. Shi, J. Dai, and J. Lian, "Ellipsometric study of the complex optical constants of a $CsPbBr_3$ perovskite thin film," J. Mater. Chem. C **6**, 10450–10455 (2018).
15. M. van Eerden, M. Jaysankar, A. Hadipour, T. Merckx, J. J. Schermer, T. Aernouts, J. Poortmans, and U. W. Paetzold, "Optical Analysis of Planar Multicrystalline Perovskite Solar Cells," Adv. Opt. Mater. **5**, 1700151 (2017).
16. Q. Lin, A. Armin, R. C. R. Nagiri, P. L. Burn, and P. Meredith, "Electro-optics of perovskite solar cells," Nat. Photonics **9**, 106–112 (2015).
17. M. Jošt, E. Köhnen, A. B. Morales-Vilches, B. Lipovšek, K. Jäger, B. Macco, A. Al-Ashouri, J. Krč, L. Korte, B. Rech, R. Schlatmann, M. Topič, B. Stannowski, and S. Albrecht, "Textured interfaces in monolithic perovskite/silicon tandem solar cells: advanced light management for improved efficiency and energy yield," Energy Environ. Sci. **11**, 3511–3523 (2018).
18. Z. Xie, S. Sun, Y. Yan, L. Zhang, R. Hou, F. Tian, and G. G. Qin, "Refractive index and extinction coefficient of $NH_2CH=NH_2PbI_3$ perovskite photovoltaic material," J. Phys. Condens. Matter **29**, 245702 (2017).
19. E. Raoult, R. Bodeux, S. Jutteau, S. Rives, A. Yaiche, D. Coutancier, J. Rousset, and S. Collin, "Optical Characterizations and Modelling of Semitransparent Perovskite Solar Cells for Tandem Applications," 36th Eur. Photovolt. Sol. Energy Conf. Exhib. 757-763 (2019).
20. E. Raoult, R. Bodeux, S. Jutteau, S. Rives, A. Yaiche, D. Coutancier, J. Rousset, and S. Collin, "Optical analysis and optimizations of semi-transparent triple cation perovskite solar cells for tandem applications," in *Physics, Simulation, and Photonic Engineering of Photovoltaic Devices IX*, A. Freundlich, M. Sugiyama, and S. Collin, 11 (2020).
21. G. F. Burkhard, E. T. Hoke, and M. D. McGehee, "Accounting for Interference, Scattering, and Electrode Absorption to Make Accurate Internal Quantum Efficiency Measurements in Organic and Other Thin Solar Cells," Adv. Mater. **22**, 3293–3297 (n.d.).
22. M. Rubin, "Optical properties of soda lime silica glasses," Sol. Energy Mater. **12**, 275–288 (1985).
23. M. Herzberger, "The Dispersion of Optical Glass*," J. Opt. Soc. Am. **32**, 70 (1942).
24. M. C. Troparevsky, A. S. Sabau, A. R. Lupini, and Z. Zhang, "Transfer-matrix formalism for the calculation of optical response in multilayer systems: from coherent to incoherent interference," Opt. Express **18**, 24715 (2010).
25. R. Santbergen, A. H. M. Smets, and M. Zeman, "Optical model for multilayer structures with coherent, partly coherent and incoherent layers," Opt. Express **21**, A262 (2013).
26. A. R. Forouhi and I. Bloomer, "Optical properties of crystalline semiconductors and dielectrics," Phys. Rev. B **38**, 1865–1874 (1988).
27. A. R. Forouhi and I. Bloomer, "Optical dispersion relations for amorphous semiconductors and amorphous dielectrics," Phys. Rev. B **34**, 7018–7026 (1986).
28. G. Legeay, "Couches minces amorphes d'ITO : caractérisation, structure, évolution et fonctionnalisation sous rayonnements UV.," PHD thesis, Université Rennes 1 (2011).
29. J. O. Park, J. H. Lee, J. J. Kim, and S.-H. Cho, "Observation of Crystallization Behavior in ITO Thin Films Prepared by RF-Magnetron Sputtering with and without External Heating," Mater. Sci. Forum **449–452**, 481–484 (2004).
30. T. J. Vink, W. Walrave, J. L. C. Daams, P. C. Baarslag, and J. E. A. M. van den Meerakker, "On the homogeneity of sputter-deposited ITO films Part I. Stress and microstructure," Thin Solid Films **266**, 145–151 (1995).
31. S. Bhagwat and R. P. Howson, "Use of the magnetron-sputtering technique for the control of the properties of indium tin oxide thin films," Surf. Coat. Technol. **111**, 163–171 (1999).
32. H. Liu, H. Liu, J. Yang, F. Yang, Z. Liu, and S. M. Jain, "Improving the Performance of Planar Perovskite Solar Cells through a Preheated, Delayed Annealing Process To Control Nucleation and Phase Transition of Perovskite Films," Cryst. Growth Des. **19**, 4314–4323 (2019).
33. G. E. Jellison and F. A. Modine, "Parameterization of the optical functions of amorphous materials in the interband region," Appl. Phys. Lett. **69**, 371–373 (1996).
34. G. Xing, N. Mathews, S. Sun, S. S. Lim, Y. M. Lam, M. Gratzel, S. Mhaisalkar, and T. C. Sum, "Long-Range Balanced Electron- and Hole-Transport Lengths in Organic-Inorganic CH3NH3PbI3," Science **342**, 344–347 (2013).
35. H. Li, C. Cui, X. Xu, S. Bian, C. Ngaojampa, P. Ruankham, and A. P. Jaroenjittchai, "A review of characterization of perovskite film in solar cells by spectroscopic ellipsometry," Sol. Energy **212**, 48–61 (2020).

36. C. G. Bailey, G. M. Piana, and P. G. Lagoudakis, "High-Energy Optical Transitions and Optical Constants of $CH_3NH_3PbI_3$ Measured by Spectroscopic Ellipsometry and Spectrophotometry," J. Phys. Chem. C **123**, 28795–28801 (2019).
37. J. Szczyrbowski, "Determination of optical constants of real thin films," J. Phys. Appl. Phys. **11**, 583–593 (1978).
38. G. Yin, C. Merschjann, and M. Schmid, "The effect of surface roughness on the determination of optical constants of $CuInSe_2$ and $CuGaSe_2$ thin films," J. Appl. Phys. **113**, 213510 (2013).
39. K.-D. Jäger, O. Isabella, A. H. M. Smets, R. A. C. M. M. van Swaaij, and M. Zeman, *Solar Energy: Fundamentals, Technology and Systems,* UIT Cambridge (2016).
40. A. Flat and A. G. Milnes, "Optimization of multi-layer front-contact grid patterns for solar cells," Sol. Energy **23**, 289–299 (1979).
41. T. Kirchartz, F. Deledalle, P. S. Tuladhar, J. R. Durrant, and J. Nelson, "On the Differences between Dark and Light Ideality Factor in Polymer:Fullerene Solar Cells," J. Phys. Chem. Lett. **4**, 2371–2376 (2013).
42. R. Kumar, J. Kumar, P. Srivastava, D. Moghe, D. Kabra, and M. Bag, "Unveiling the Morphology Effect on the Negative Capacitance and Large Ideality Factor in Perovskite Light-Emitting Diodes," ACS Appl. Mater. Interfaces **12**, 34265–34273 (2020).
43. N. Wu, Y. Wu, D. Walter, H. Shen, T. Duong, D. Grant, C. Barugkin, X. Fu, J. Peng, T. White, K. Catchpole, and K. Weber, "Identifying the Cause of Voltage and Fill Factor Losses in Perovskite Solar Cells by Using Luminescence Measurements," Energy Technol. **5**, 1827–1835 (2017).
44. M. Stolterfoht, C. M. Wolff, Y. Amir, A. Paulke, L. Perdigón-Toro, P. Caprioglio, and D. Neher, "Approaching the fill factor Shockley–Queisser limit in stable, dopant-free triple cation perovskite solar cells," Energy Environ. Sci. **10**, 1530–1539 (2017).